



## Quasi-random nonlinear scale space

Akshaya Mishra \*, Alexander Wong, David A. Clausi, Paul W. Fieguth

Vision and Image Processing Lab, University of Waterloo, Canada

### ARTICLE INFO

#### Article history:

Available online 18 January 2010

#### Keywords:

Nonlinear scale space  
Bayesian estimation  
Quasi-random  
Anisotropic diffusion  
Multi-scale  
Edge detection

### ABSTRACT

A novel nonlinear scale space framework is proposed for the purpose of multi-scale image representation. The scale space decomposition problem is formulated as a general Bayesian least-squares estimation problem. A quasi-random density estimation approach is introduced for estimating the posterior distribution between consecutive scale space realizations. In addition, the application of the proposed nonlinear scale space framework for edge detection is proposed. Experimental results demonstrate the effectiveness of the proposed scale space framework for constructing scale space representations with significantly better structural localization across all scales when compared to state-of-the-art scale space frameworks such as anisotropic diffusion, regularized nonlinear diffusion, complex nonlinear diffusion, and iterative bilateral scale space methods, especially under scenarios with high noise levels.

© 2010 Elsevier B.V. All rights reserved.

### 1. Introduction

An interesting phenomenon pertaining to the physical world is that it is composed of a plethora of objects that are conceptually meaningful at particular scales. An example of this phenomenon is that of a house, which is conceptually meaningful when considered from the meter scale, but not at the centimeter or kilometer scales. At the centimeter scale, it might be more appropriate to discuss the bricks that make up the house, likewise at the kilometer scale the neighborhood in which the house resides. Similarly, when imaging the physical world, different image structures are meaningful only in the context of certain scales. Therefore, we are motivated to develop multi-scale methods for decomposing images at different scales for the purposes of modeling, description, and analysis.

A powerful approach for multi-scale image decomposition is scale space theory (Witkin, 1983), where image structures at different scales within an image are handled by representing the image as a single-parameter family of images, with a progressive decrease in fine scale structures between successive scales. Scale space theory has proven to be useful for a wide variety of image processing and computer vision applications such as denoising (Yu et al., 2008; Ling and Bovik, 2002; Gilboa et al., 2004; Gilboa, 2008), edge detection (Lindberg, 1996; Perona and Malik, 1990; Catte et al., 1992; Yu et al., 2008), color enhancement (Jobson et al., 1997), segmentation (Maeda et al., 1998; Pathak et al.,

2000; Manmatha and Rothfeder, 2005; Petrovic et al., 2004; Wong et al., 2009), and blur estimation (Elder and Zucker, 1996, 1998).

Witkin (1983) and Koenderink and Van Doorn (1984) first proposed the linear scale space framework, where an image is decomposed into a family of images, each produced by convolving the original image with a Gaussian function conditioned by the associated scale parameter. While computationally efficient, the linear scale space framework produces scale space representations with poorly localized image structures and high inter-region structure smoothing at larger scales. To address these issues associated with poor structural localization and inter-region structure smoothing, Perona and Malik (1990) proposed a nonlinear scale space framework based on the generalized diffusion equation as a function of gradient magnitude. By encouraging diffusion between pixels with similar structural characteristics, structural localization at coarse scales is improved. Unfortunately, while noticeably better than the linear scale space framework, significant structural delocalization and inter-region structure smoothing still persists at coarser scales.

Recent work in scale space frameworks has focused on improving upon the generalized diffusion approach proposed by Catte et al. (1992) proposed that the posedness of the problem formulated by Perona and Malik can be improved by regularizing the conduction coefficient using Gaussian regularization priors. Yu et al. (2008) improved upon this regularization scheme through the use of radial-basis function kernels, which also provides better structural separability. Black et al. (1998) proposed that the posedness of the problem can also be improved through the use of a conduction coefficient based on robust statistics. Gilboa et al. (2004) extended the generalized diffusion equation

\* Corresponding author. Fax: +1 5198851211.

E-mail addresses: [akmishra@uwaterloo.ca](mailto:akmishra@uwaterloo.ca) (A. Mishra), [a28wong@uwaterloo.ca](mailto:a28wong@uwaterloo.ca) (A. Wong), [dclausi@uwaterloo.ca](mailto:dclausi@uwaterloo.ca) (D.A. Clausi), [pfieguth@uwaterloo.ca](mailto:pfieguth@uwaterloo.ca) (P.W. Fieguth).

used by Perona and Malik into the complex domain by combining nonlinear diffusion and the free Schrödinger equation to better preserve ramp characteristics in images. Unfortunately, despite such advancements in scale space theory, the issues associated with structural localization persists at coarser scales. Furthermore, existing scale space frameworks are highly sensitive to the presence of noise and as such generally produce unsatisfactory scale space representations of images characterized by high noise levels, which will be illustrated in the experimental results.

The main contribution of this paper is a novel and effective nonlinear scale space framework based on Bayesian estimation theory. By formulating scale space decomposition using general Bayesian least squares approach, an efficient solution is provided using a quasi-random density estimation approach based on a set of objective functions and criteria designed to promote structural localization at all scales. Furthermore, we demonstrate how the proposed scale space framework can be used for robust edge detection. This paper is organized as follows. The scale space decomposition problem is formulated in Section 2. A quasi-random density estimation scheme is introduced in Section 3. The application of the proposed framework for edge detection is described in Section 5. Finally, experimental results are presented in Section 6 and conclusions are drawn in Section 7.

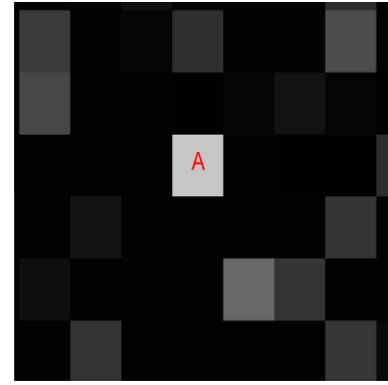


**Fig. 3.** Example of an isolated point. Point A is an outlier, because  $L^x - L_{i-1}(s) > \sigma_{L_{i-1}}$ , which implies the difference of pixel A's intensity from the intensities corresponding to the modes of its neighbor distribution are greater than the image standard deviation  $\sigma_{L_{i-1}}$ .

**2. Problem formulation**

Let  $S$  be set of sites in a discrete lattice  $\mathcal{E}$  upon which an image is defined and  $s \in S$  be a site in  $\mathcal{E}$ . Further, let the measured image

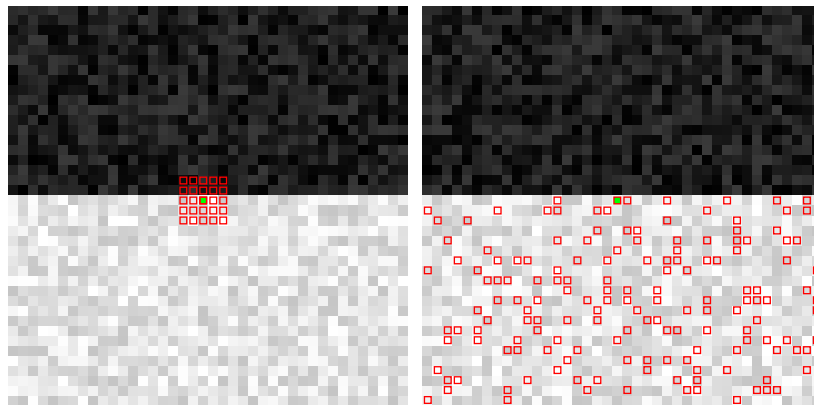


**Fig. 1.** In existing scale space representations, left, all samples within a local neighborhood are used, regardless of relevance. In the proposed scale space representation, right, only samples with high relevancy from across the representation are used to provide more robust statistical estimates.

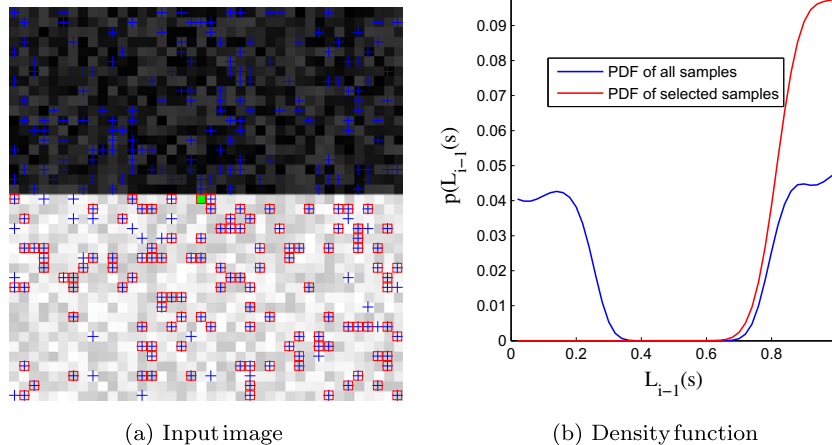


**Fig. 2.** A synthetic image, left, where the green pixel (at center) represents the estimation site, blue markers represent random samples, and red markers represent the selected samples for density estimation. The corresponding probability distribution  $p(L_{i-1}(s))$  of the green pixel is shown in (b), where blue (undesirable) PDF is based on *all* samples, whereas the red (desirable) distribution is taken over the selected samples. (For interpretation of the references to colour in this figure legend, the reader is referred to the web version of this article.)

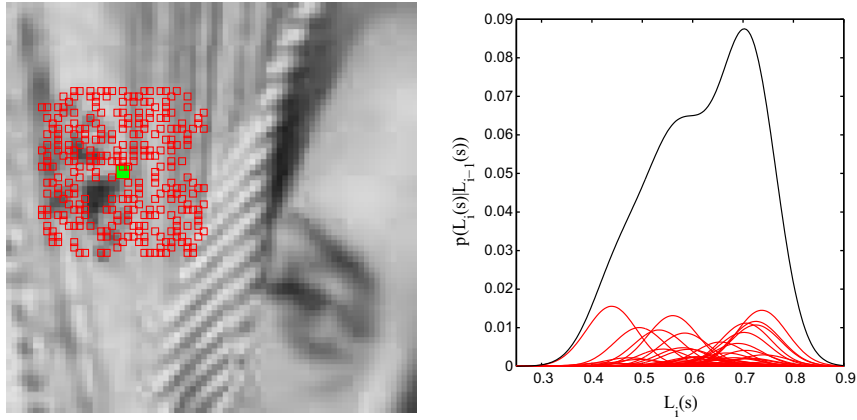


**Fig. 4.** Example estimate of  $p(L_i(s)|L_{i-1}(s))$  for a site of Barbara image. The green pixel and red squares, left, represent the site  $s$  and samples, respectively. Each sample contributes (red, right) to the overall estimated  $p(L_i(s)|L_{i-1}(s))$  (black). (For interpretation of the references to colour in this figure legend, the reader is referred to the web version of this article.)

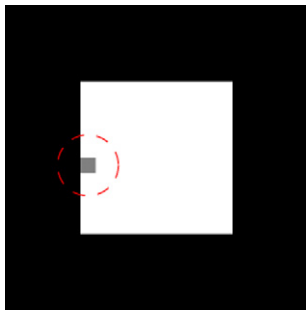


**Fig. 5.** An ideal synthetic image used to explain the physical significance of the three objective functions ( $f_1$ ,  $f_2$ , and  $f_3$ ) of (7). The gray pixel inside the dotted red circle represents the site of interest, for which the weights are shown in Fig. 6. (For interpretation of the references to colour in this figure legend, the reader is referred to the web version of this article.)

$I = \{I(s)|s \in S\}$ , gradient  $G_i = \{G_i(s)|s \in S\}$ , scale space representation  $L_i = \{L_i(s)|s \in S\}$ , and residual fine scale structure  $C_i = \{C_i(s)|s \in S\}$  be random fields on  $S$ . Initializing with  $L_0(s) = I(s)$ ,

the scale space decomposition relationship can be expressed as a recursion

$$L_{i-1}(s) = L_i(s) + C_i(s), \tag{1}$$

such that we interpret  $C$  as the inter-scale residual. Given (1) one can view the computation of  $L_i(s)$  as an inverse problem and, as such, can be solved as an estimation problem. Given the “measurement”  $L_{i-1}(s)$ , and modeling the fine-scale residual  $C_i(s)$  as “noise”, we can estimate the state  $L_i(s)$  as the Bayesian least-squares estimate (BLSE):

$$\hat{L}_i(s) = \arg_{L_i} \min \left\{ E \left( \left( \hat{L}_i(s) - L_i(s) \right)^2 \middle| L_{i-1}(s) \right) \right\}. \tag{2}$$

Minimizing (2) gives

$$\hat{L}_i(s) = \underbrace{\int L_i(s) p(L_i(s)|L_{i-1}(s)) dL_i(s)}_{E(L_i(s)|L_{i-1}(s))}, \tag{3}$$

implying that the optimal estimate of scale space representation  $L_i(s)$  is the mean conditioned on the previous scale space representation  $L_{i-1}(s)$ . Because the conditional mean of  $\hat{L}_i(s)$  can be a highly

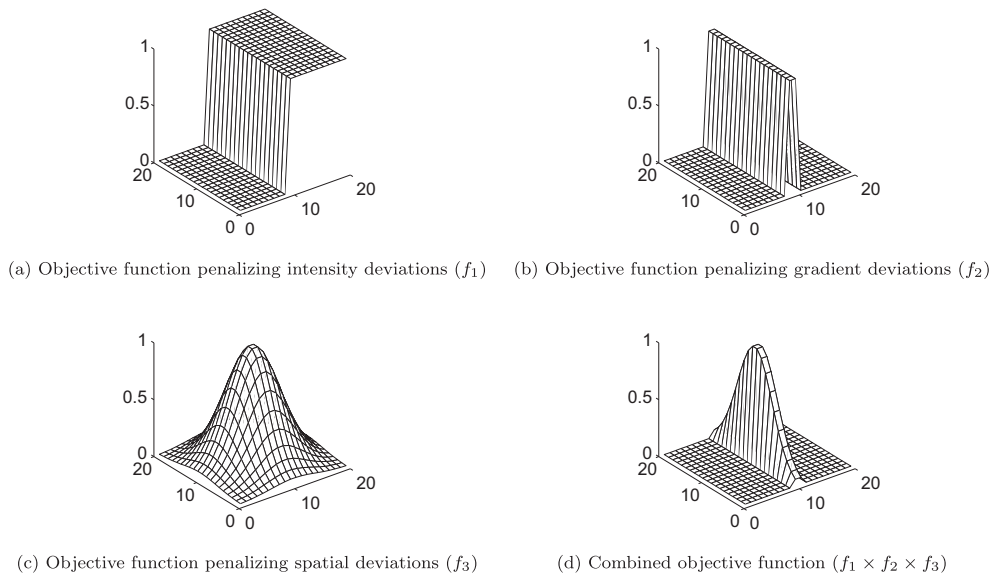


**Fig. 6.** The physical significance of the three objective functions ( $f_1$ ,  $f_2$  and  $f_3$ ) of (7) for a particular pixel of the sample image shown in Fig. 5.

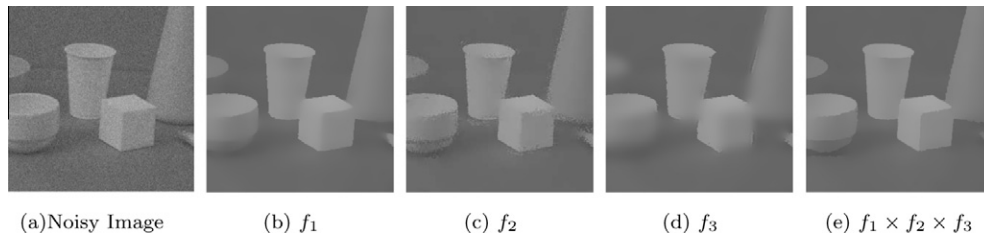


**Fig. 7.** Demonstration of the functionality of the three objective functions  $f_1$ ,  $f_2$  and  $f_3$  on the performance of proposed scale space representation using an example noisy image ( $\sigma = 10\%$ ). Columns 2–5 present the scale space representation at the sixth scale using only  $f_1$ ,  $f_2$ ,  $f_3$  individually, and then the proposed  $f_1 \times f_2 \times f_3$  as objective functions of (7).

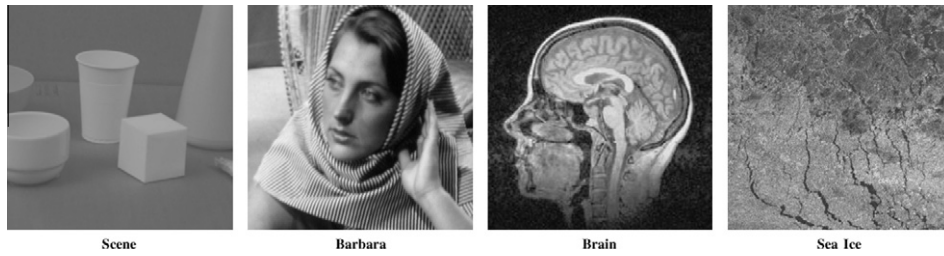


**Fig. 8.** Set of test images.

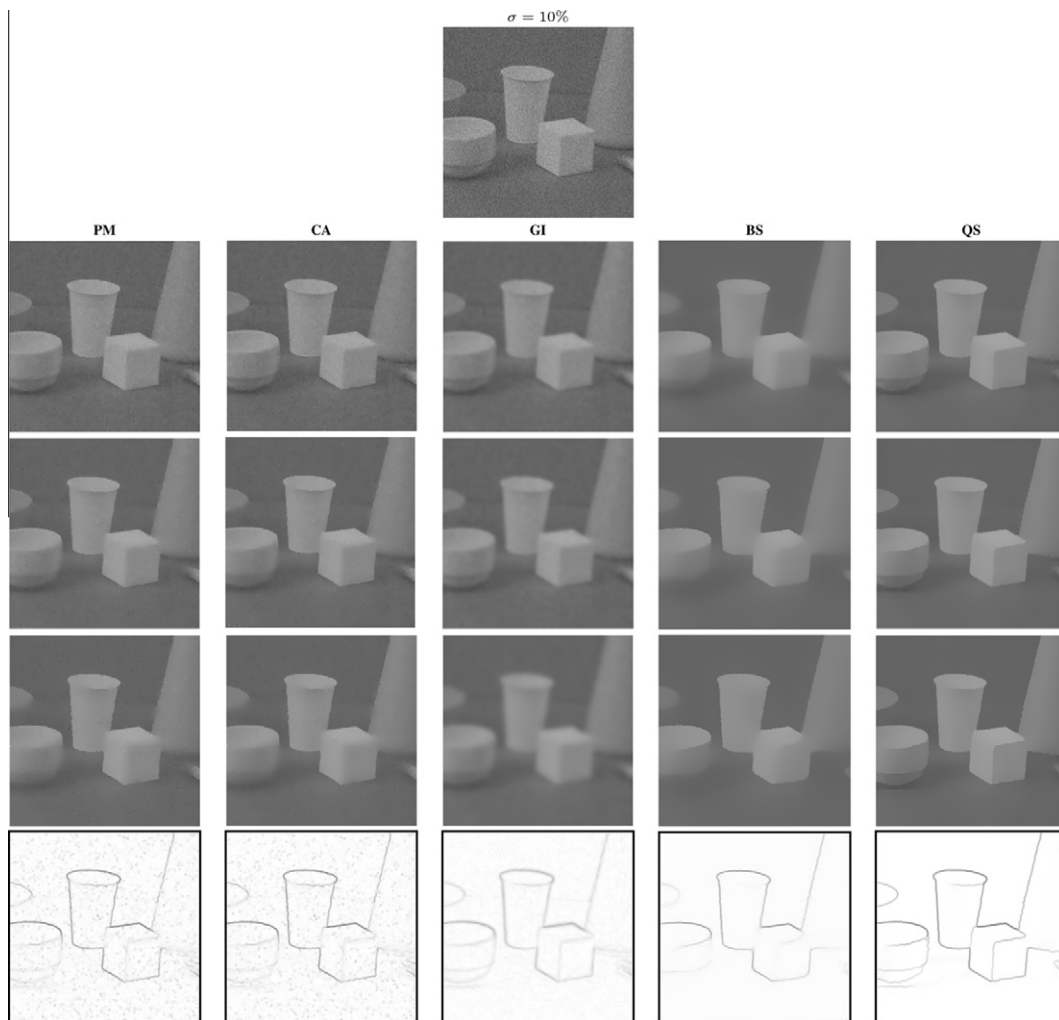


**Fig. 9.** The scale space representations of the “Scene” image for PM (Perona and Malik, 1990), CA (Catté et al., 1992), GI (Gilboa et al., 2004), BS (Wong et al., 2009), and QS under additive Gaussian noise with a standard deviation of  $\sigma = \{10\%$  of the dynamic range of the image. The scale space representations are shown with increasing  $t$  from top to bottom. The corresponding edge strength maps  $r$  from (17) are shown in the bottom row.

complicated and nonlinear function of  $L_{i-1}(s)$ , typically simpler Bayesian linear least-squares estimators (Lee, 1986) and estimators based on specific parametric posterior distribution models (Lopes et al., 1993) have been used instead. However, given the complex, nonlinear nature of images, such estimators provide poor structural decomposition and hence result in significant loss of structural detail between scale space representations. To address these issues, we propose instead to employ a quasi-random density estimation approach to estimate the conditional mean  $\hat{L}_i(s)$ . The proposed method allows for a more robust statistical estimate of  $\hat{L}_i(s)$  by rejecting outlier samples and utilizing only samples from across  $L_{i-1}(s)$  with high relevancy. This approach is fundamentally different than that used for existing scale space representations, where all samples within a local neighborhood are used, as illustrated in Fig. 1.

### 3. Quasi-random density estimation

Our goal is to obtain a robust estimate of  $p(L_i(s)|L_{i-1}(s))$  from the image intensity, gradient and spatial similarity, using a quasi-random density estimation approach, which can be described as follows. To estimate  $p(L_i(s)|L_{i-1}(s))$ , we first draw  $n$  samples from a Sobol quasi-random sequence (Sobol, 1997; von Neumann, 1951) with respect to site  $s$  at scale  $i$ . A quasi-random sampling approach is used to allow samples with low discrepancies to be drawn. Let

$L_{i-1}(s_j), j \in [1, n]$  be the intensity of the  $j$ th drawn sample of site  $s$  at scale  $i - 1$ . To utilize only samples with high relevancy, the distribution  $p(L_i(s))$  is determined to study the distribution of the samples and identify samples that are realizations of  $p(L_i(s)|L_{i-1}(s))$ . An example probability distribution  $p(L_{i-1}(s))$  at a particular scale is shown in Fig. 2b .

To form a Gaussian mixture model of  $p(L_{i-1}(s))$ , the modes of the distribution are determined in the following manner. The local maxima of  $p(L_{i-1}(s))$  are detected, denoted as  $L^K = \{L_{i-1}^{K_1}(s), L_{i-1}^{K_2}(s), \dots, L_{i-1}^{K_k}(s)\}$  for  $\kappa_k$  maxima. The distribution  $p(L_{i-1}(s))$  can then be modeled as a Gaussian mixture model, with the means and variances of the individual Gaussian distributions defined by  $L^K$  and  $\sigma_{L_{i-1}}^2$  (usually the noise variance at scale  $i$ ), respectively. To determine the realizable sample set  $\Omega$ , we first identify the Gaussian distribution to which  $L_{i-1}(s)$  belongs by finding the highest local maximum of  $p(L_{i-1}(s))$  within one standard deviation of  $L_{i-1}(s)$ ,

$$L^\gamma = \max(L^K), \quad \text{where } L_{i-1}(s) - \sigma_{L_{i-1}} \leq L^K \leq L_{i-1}(s) + \sigma_{L_{i-1}}. \quad (4)$$

Based on the identified Gaussian distribution to which  $L_{i-1}(s)$  belongs, with a mean of  $L^\gamma$  and a variance of  $\sigma_{L_{i-1}}^2$ , all samples within  $\sigma_{L_{i-1}}$  of  $L^\gamma$  are accepted as realizations:

$$\Omega = \{s_j \ni |L_{i-1}(s_j) - L^\gamma| < \sigma_{L_{i-1}}\}, \quad (5)$$

restricting the realizable sample set of  $p(L_i(s)|L_{i-1}(s))$  to those samples with high statistical relevancy to  $L_{i-1}(s)$ .

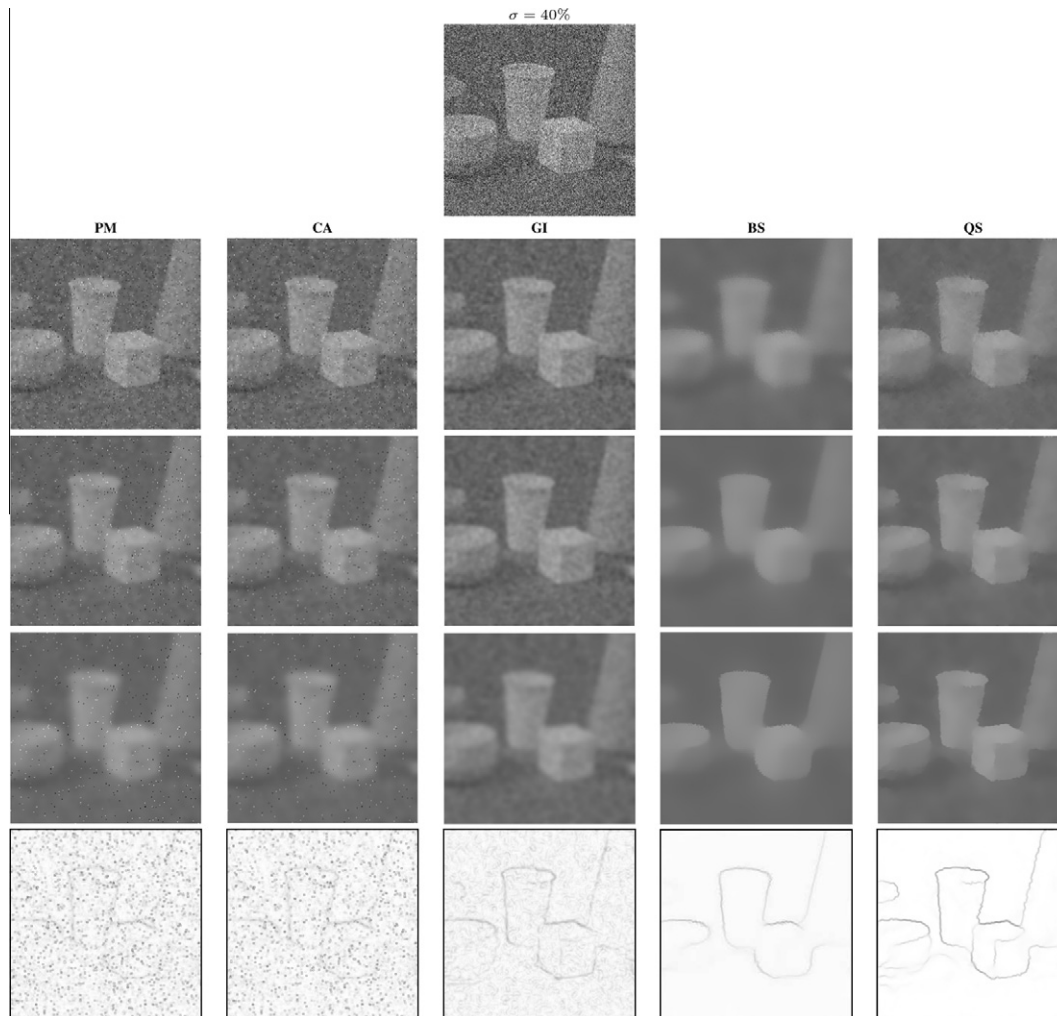


Fig. 10. The scale space representations of the “Scene” image, as in Fig. 9, but with a noise standard deviation of  $\sigma = \{40\%$  of the dynamic range of the image. Observe the significant noise reduction and good localization of the edge map for the QS method.

Now, given the selected sample set  $\Omega$ , we wish to define the estimated posterior distribution  $\hat{p}(L_i(s)|L_{i-1}(s))$ ,

$$\hat{p}(L_i(s)|L_{i-1}(s)) = \frac{p^*(L_i(s)|L_{i-1}(s))}{\int_0^1 p^*(L_i(s)|L_{i-1}(s)) dL_i(s)}, \quad (6)$$

based on some distribution  $p^*$ , which measures the relevance of each sample to the estimation of  $L_i(s)$ . We propose

$$p^*(L_i(s)|L_{i-1}(s)) = \frac{1}{\sqrt{2\pi}\sigma_{L_i}} \sum_{k \in \Omega} f_1(k)f_2(k)f_3(k) \exp\left(-\frac{1}{2} \left(\frac{L_i - L_{i-1}(s_k)}{\sigma_{L_{i-1}}}\right)^2\right), \quad L_i \in [0, 1], \quad (7)$$

where  $f_1(k)$ ,  $f_2(k)$ , and  $f_3(k)$  are objective functions, assessing sample relevance, on the basis of intensity, gradient, and spatial offset, respectively:

$$f_1(k) = \exp\left(-\frac{1}{\rho_{I_{i-1}}}(L_{i-1}(s) - L_{i-1}(s_k))^2\right), \quad (8)$$

$$f_2(k) = \exp\left(-\frac{1}{\rho_{G_{i-1}}}(G_{i-1}(s) - G_{i-1}(s_k))^2\right), \quad (9)$$

and

$$f_3(k) = \exp\left(-\frac{1}{\rho_{V_{i-1}}}\|V_{i-1}(s) - V_{i-1}(s_k)\|_2\right). \quad (10)$$

$G$  is the image gradient, computed using a first difference operator, and  $V$  represents the spatial location. The terms  $\rho_{I_{i-1}}$ ,  $\rho_{G_{i-1}}$  and  $\rho_{V_{i-1}}$  are regularization constants for scale  $i - 1$ , where spatial parameter  $\rho_{V_{i-1}}$  is user-specified, and  $\rho_{I_{i-1}}$ ,  $\rho_{G_{i-1}}$  are calculated as the median over local standard-deviations computed over a sliding window:

$$\rho_{I_{i-1}} = \text{median}(\sigma_{I_{i-1}}(j, k)), \quad (11)$$

$$\rho_{G_{i-1}} = \text{median}(\sigma_{G_{i-1}}(j, k)). \quad (12)$$

An example of an estimate of  $p(L_i(s)|L_{i-1}(s))$  for a site in the Barbara image is shown in Fig. 4.

The physical significance of the three objective functions ( $f_1$ ,  $f_2$ ,  $f_3$ ) can be explained using an example. Given a pixel of interest, marked in Fig. 5, the values of the objective functions for the neighboring samples are presented in Fig. 6. The objective function penalizing intensity deviations,  $f_1$ , is designed to enforce intensity similarity. As shown in Fig. 6a,  $f_1$  reflects the steep intensity edge of Fig. 5. The objective function penalizing gradient deviations,  $f_2$ , is designed to enforce gradient similarity, which allows for better preservation of structural boundaries. As shown in Fig. 6b, the values associated with  $f_2$  reflect the local ridge of high gradient which passes next to the marked pixel in Fig. 5. Finally, the objective function penalizing spatial deviations,  $f_3$ , is designed to enforce spatial locality, which is based on the intuition that spatially neighboring pixels are similar to each other. As shown in Fig. 5c, the values associated with  $f_3$  form a Gaussian function, with a decreasing weight with increasing spatial separation. The value of the



Fig. 11. The scale space representations of the “Barbara” image, with a  $\sigma = \{10\%$  noise level as in Fig. 9. Observe the significant absence of blurring in the QS representations.

combined objective function ( $f_1 \times f_2 \times f_3$ ) is shown in Fig. 6d, where intensity similarity, gradient similarity, and spatial locality are simultaneously enforced.

The functionality of the three objective functions  $f_1, f_2$  and  $f_3$  is demonstrated using an example noisy image in Fig. 7. Using only the objective function penalizing spatial deviations ( $f_3$ ) results in significant structural delocalization (Fig. 7d), while using only the objective function penalizing gradient deviations ( $f_2$ ) results in improved structural localization but poor continuity between structural boundaries (Fig. 7c). The combination of the three objectives functions ( $f_1 \times f_2 \times f_3$ ) gives the best result by providing strong structural localization and continuity between structural boundaries (Fig. 7e).

A special case occurs when ( $L^k - L_{i-1}(s) > \sigma_{L_{i-1}}$ ), meaning that the site  $s$  does not fit into the Gaussian mixture model for  $p(L_i(s))$ , implying that all of the neighbors of site  $s$  are completely dissimilar with  $s$ . This situation is more frequent for images that are contaminated with salt and pepper noise, such as the example in Fig. 3. In this special case the site is considered as an outlier, an all samples are accepted as realizations,  $\Omega = \{s_j\}$ , and  $p^*$  in (7) becomes an unweighted average:

$$p^*(L_i(s)|L_{i-1}(s)) = \frac{1}{\sqrt{2\pi}\sigma_{L_i}} \sum_{k \in \Omega} \exp\left(-\left(\frac{L_i - L_{i-1}(s_k)}{2\sigma_{L_{i-1}}}\right)^2\right). \quad (13)$$

#### 4. Relation to anisotropic diffusion

There is a relationship between the proposed quasi-random scale space and the anisotropic diffusion scale space formulation (Perona and Malik, 1990), where the latter diffusion can be expressed as

$$\frac{\partial L(s, i)}{\partial i} = \text{div}(g(\|\nabla L\|)\nabla L), \quad (14)$$

where  $\|\nabla L\|$  is the gradient magnitude and  $g$  is an edge stopping function. The function  $g$  is chosen such that  $g(x) \rightarrow 0$  as  $x \rightarrow 0$ . The solution to (14) in discrete form can be written as

$$L_i(s) = L_{i-1}(s) + \frac{\lambda}{|\Omega_s|} \sum_{k \in \Omega_s} g(\|L_{i-1}(k) - L_{i-1}(s)\|)(L_{i-1}(k) - L_{i-1}(s)), \quad (15)$$

where  $|\Omega_s|$  is the number of neighboring pixels and the term  $\lambda$  is a user-defined constant. Defining  $C_i$  to be the difference in (15),

$$C_i(s) = -\frac{\lambda}{|\Omega_s|} \sum_{k \in \Omega_s} g(\|L_{i-1}(k) - L_{i-1}(s)\|)(L_{i-1}(k) - L_{i-1}(s)), \quad (16)$$

the scale space decomposition expressed in (1) for the proposed scale space formulation is seen to share a similar form with that

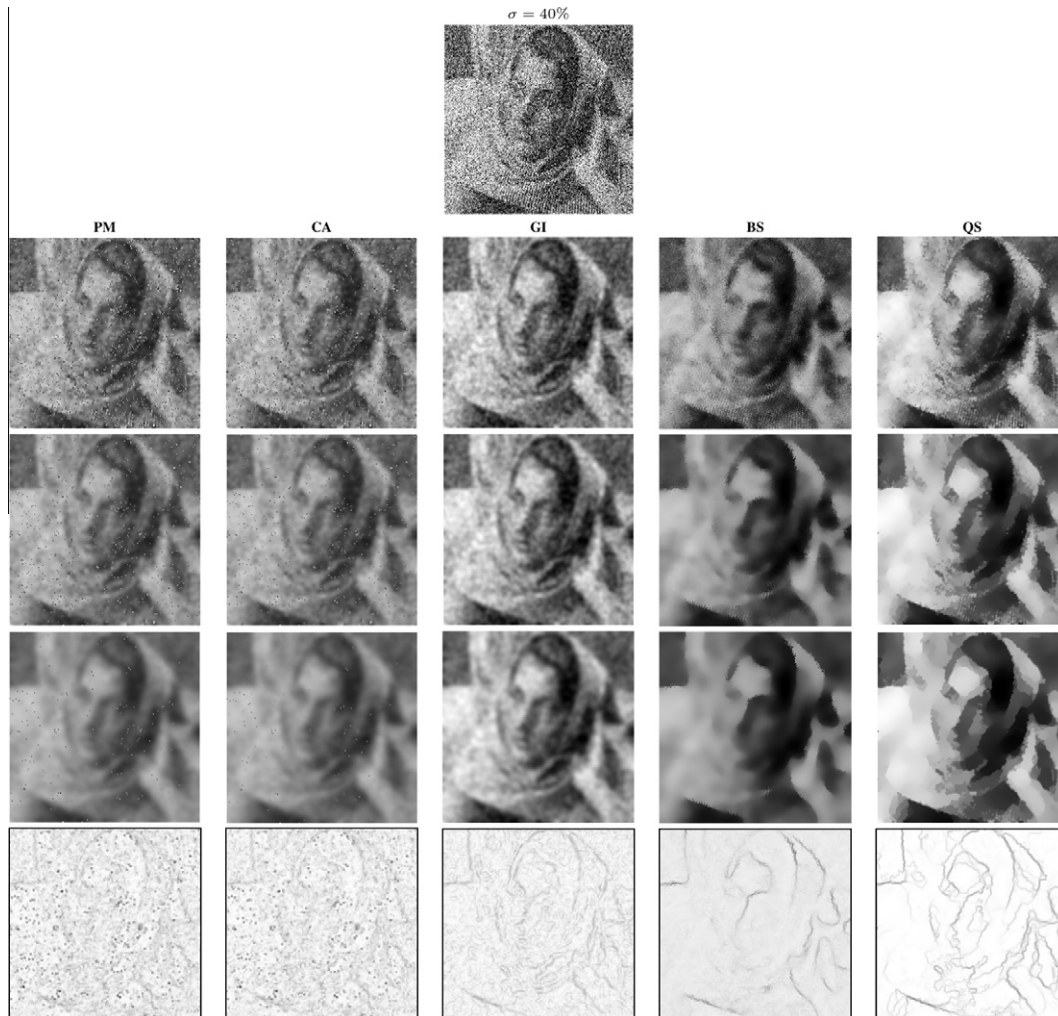


Fig. 12. The scale space representations of the “Barbara”, as in Fig. 11, but with a higher noise standard deviation of  $\sigma = \{40\%$ . Observe the presence of blurring and noise outliers between QS and the compared methods.

of anisotropic diffusion. There are two major differences, however, that greatly affect the resulting scale space realizations. The anisotropic diffusion formulation is a purely local in nature, and as such can be expressed as a partial differential equation as shown in (14), whereas the proposed quasi random formulation utilizes a stochastic, *non-local* paradigm, and as such admits models which cannot be expressed in the form of (14). Similarly, the behaviour of (14) is controlled by a single function  $g$ , a function of the gradient at a point, whereas our proposed approach permits a considerably more flexible set of criteria, controlled by three functions of intensity, gradient, and location. By utilizing relevant samples from across the image in a stochastic manner, the quasi-random scale space provides better structural decomposition without significant loss in structural detail between scales.

### 5. Application to edge detection

The quasi-random nonlinear scale space framework can be applied to the problem of edge detection. Construct a map  $r = \{r_s | s \in S\}$ , where  $R = \{R_s | s \in S\}$  is a random field on  $S$ , with  $R_s$  taking on values representing the edge strength at pixel  $s$ . Intuitively, edges that exist across multiple scales should be weighted

higher than edges that exist only at a few scales. Therefore, a simple approach to computing the edge strength  $r$  at site  $s$  is to compute the sum of gradient magnitude across all scales of  $L_i(s)$ ,

$$r(s) = \sum_i |\nabla L_i(s)|, \tag{17}$$

where  $\nabla$  represents a first order Sobel edge detector operator.

While this multi-scale edge detection scheme applies to all existing scale space frameworks, based on testing to date it is particularly effective when used with the quasi-random nonlinear scale space framework given the structural localization and noise robustness at all scales. The experimental result for multi-scale edge strength obtained using (17) is presented in Section 6.

### 6. Experiments

To study the effectiveness of the quasi-random nonlinear scale space framework for constructing multi-scale representations with well localized structures at all scales, two sets of experiments were performed based on the multi-scale decomposition of a set of four test images under different scenarios. The set of test images, shown in Fig. 8, consists of two natural images (Scene and Barbara), a

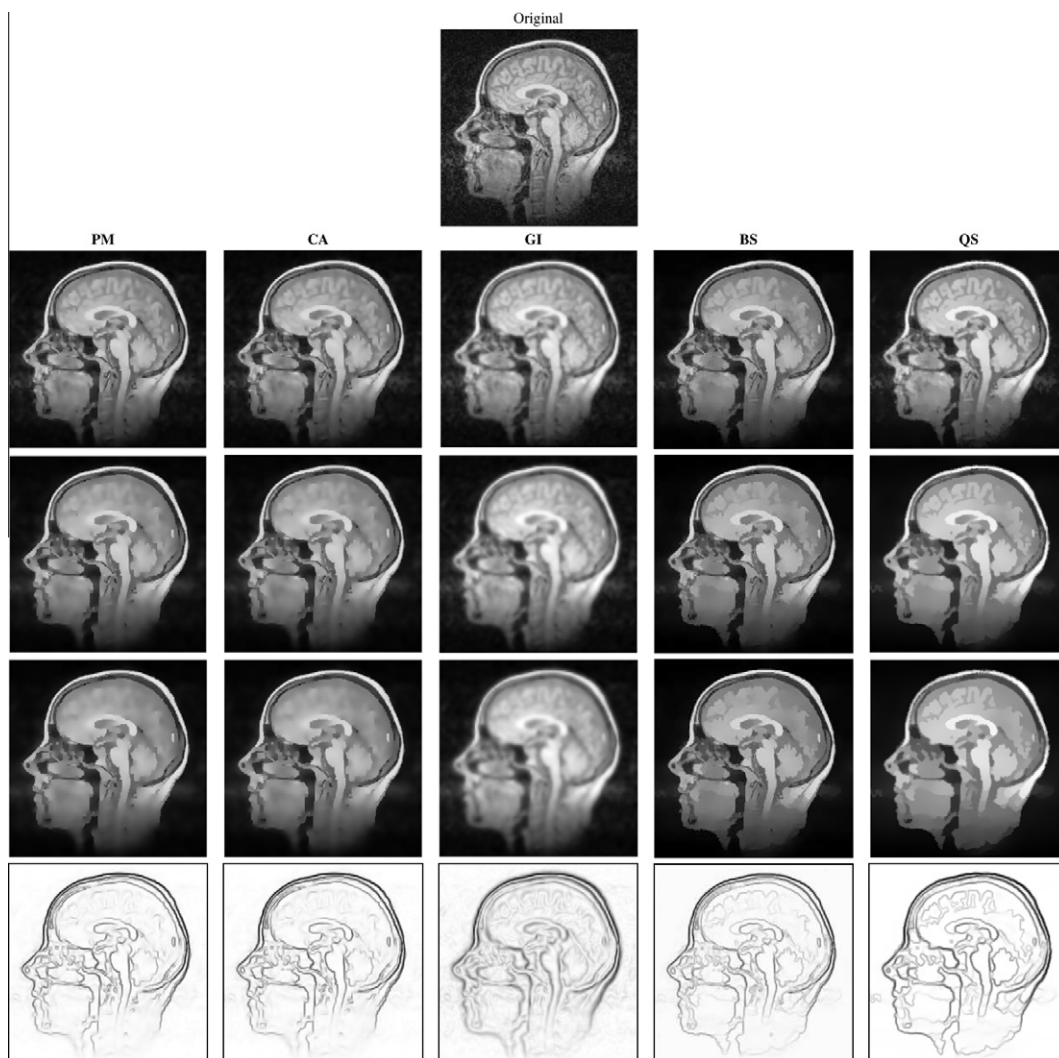


**Fig. 13.** The scale space representation of the tested scale space frameworks for a clinical MR image. For PM and CA, the scale space representations are shown for  $t = \{15, 35, 50\}$ . For GI, the scale space representations are shown for  $t = \{10, 15, 35\}$ . For QS, the scale space realizations are shown for  $t = \{2, 4, 6\}$ . The scale space representations are shown with increasing  $t$  from top to bottom. The corresponding edge strength maps  $r$  are shown in the bottom row. Observe the absence of blurring in the QS representations, particularly in the brain regions.

clinical magnetic resonance (MR) brain image (Brain), and a satellite (RADARSAT-1) synthetic aperture radar (SAR) sea-ice image (Sea Ice) from the Canadian Ice Service. The nonlinear diffusion scale space frameworks proposed by Perona and Malik (1990) (PM), the regularized nonlinear diffusion scale space proposed by Catte et al. (1992) (CA), the complex nonlinear diffusion scale space proposed by Gilboa et al. (2004) (GI), and the iterative bilateral scale space used by Wong et al. (2009) (BS) were evaluated for comparison purposes, with all parameters used during testing based on the respective papers. The proposed quasi-random nonlinear scale space framework will be denoted as QS, with the following parameters:  $n = 100$  samples, window size  $w = 12$ , and a spatial deviation regularization constant of  $\rho_{V_{t-1}} = 6$  pixels. The  $n$  samples were collected from a spatial radius of 18 pixels.

### 6.1. Experiment 1: noise sensitivity

To study the noise sensitivity of the proposed scale space framework, the “Scene” and “Barbara” images were contaminated by additive Gaussian noise with standard deviations of  $\sigma = \{10\%, 40\%\}$  of the dynamic range of the images. The noise contaminated versions of the test images under the different noise levels are shown in top rows of Figs. 9–12.

The scale space representations of the test images at three different scales constructed using each scale space framework, along with the respective edge strength maps, are shown for the two different additive Gaussian noise levels. The scales shown for each tested framework were chosen such that they have similarly scaled structures: for PM and CA, the scale space representations are shown for  $t = 15, 35, 50$ , for GI, the scale space representations are shown for  $t = 10, 15, 35$ , and for BS and QS the shown scales are  $t = 2, 4, 6$ .

While all tested frameworks were able to produce scale space representations with monotonically decreasing fine scale structures as scale increased, the scale space representations produced using QS visually exhibit significantly better structural localization at all scales when compared to PM, CA, GI, and BS. Furthermore, based on the results for both noise levels, QS is noticeably less sensitive to the presence of noise across all scales than all four compared methods. This phenomenon is most noticeable in the high noise scenarios ( $\sigma = 40\%$ ) of Figs. 10 and 12, where no noise artifacts are present at the coarser scales in the representations produced using QS. The low noise sensitivity and high structural localization of QS is further reinforced by the edge strength maps, which noticeably fewer noise artifacts and better localized edges when constructed using QS than those constructed using PM, CA, GI, and BS.

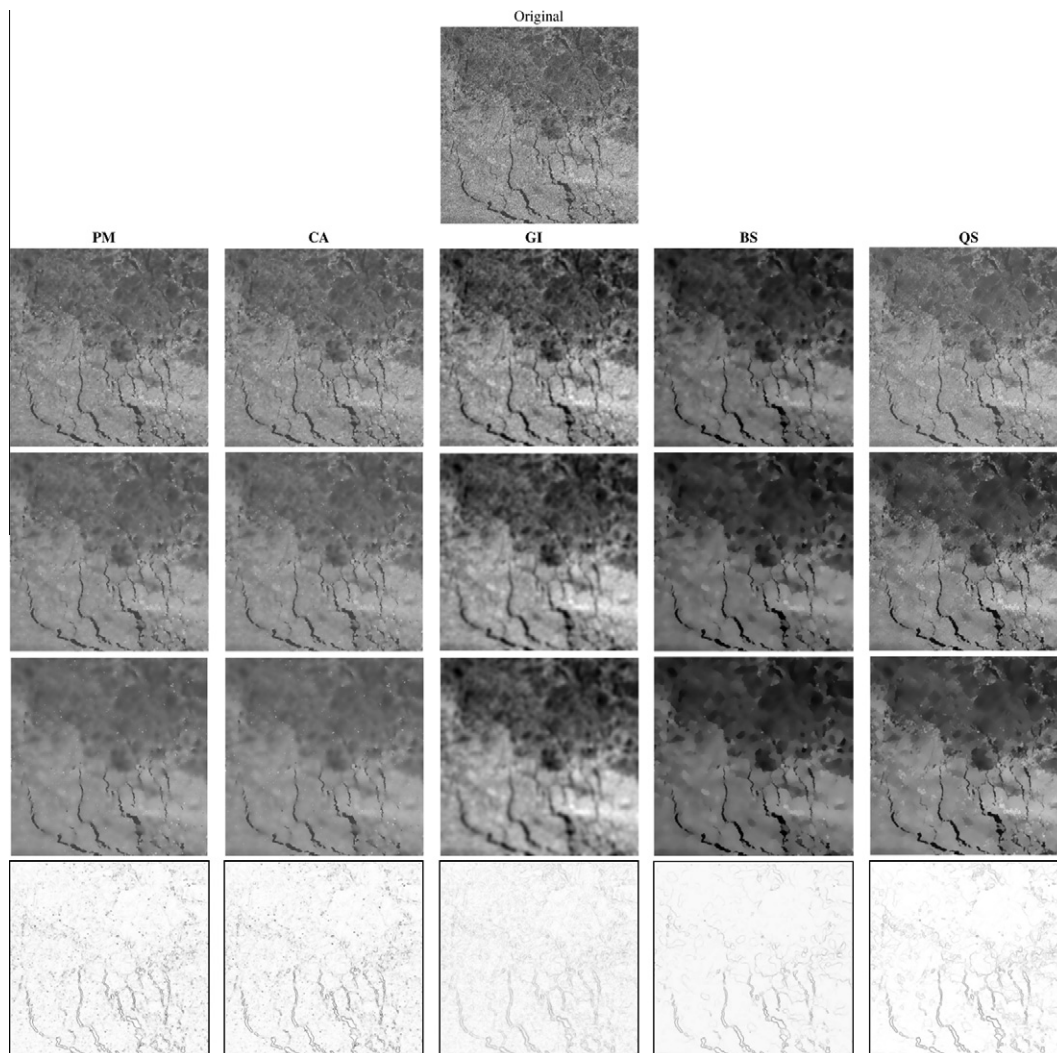


**Fig. 14.** The scale space representation of the tested scale space frameworks for a SAR sea-ice image, as in Fig. 13. Observe the improved preservation of leads (thick dark lines) in the QS representations when compared to the other tested representations. This preservation is particularly visible in the edge strength map produced using the QS representations.

## 6.2. Experiment 2: clinical MR and SAR sea-ice imagery

In the second set of experiments, shown in Fig. 13 and 14, the scale space representations of real clinical MR and SAR sea-ice imagery is studied. This set of experiments is designed to investigate the effectiveness of the various scale space frameworks in decomposing complex real-world structures under real-world noise scenarios. As with the first set of experiments, the scale space representations constructed using QS provide noticeably superior structural localization at all scales. This phenomenon is particularly noticeable in the SAR sea-ice imagery, where the structure of the leads and ridges are better localized and preserved at all scales when compared to the other tested frameworks.

## 7. Conclusions and future work

In this paper, a novel scale space framework based on Bayesian estimation theory was introduced. The formulation of the scale space decomposition problem as a general Bayesian least-squares estimation problem was presented. The limitations associated with existing scale space frameworks pertaining to structural localization and noise were addressed by solving the estimation problem using a quasi-random density estimation approach based on objective functions that promote structural localization. The application of the proposed scale space framework for the purpose of edge detection was described. Finally, experimental results demonstrated the proposed scale space framework's ability to produce scale space representations with superior structural localization when compared to state-of-the-art scale space frameworks, even under high noise levels.

## Acknowledgements

SAR sea ice image copyright Canadian Space Agency and courtesy of the Canadian Ice Service. Funding provided by Natural Sciences and Engineering Research Council (NSERC) via individual Discovery Grants and the Network of Centres of Excellence (NCE) Geomatics for Informed Decisions (GEOIDE).

## References

- Black, M., Sapiro, G., Marimont, D., Heeger, D., 1998. Robust anisotropic diffusion. *IEEE Trans. Image Process.* 7 (3), 421–432.
- Catte, F., Lions, P., Morel, M., Coll, T., 1992. Image selective smoothing and edge detection by nonlinear diffusion. *SIAM J. Numer. Anal.* 29 (1), 182–193.
- Elder, J., Zucker, S., 1996. Scale space localization, blur, and contour-based image coding. In: *Proc. IEEE Comput. Society Conf. on Computer Vision and Pattern Recognition*, pp. 27–34.
- Elder, J., Zucker, S., 1998. Local scale control for edge detection and blur estimation. *Proc. IEEE Trans. Pattern Anal. Machine Intell.* 20 (7), 699–716.
- Gilboa, G., 2008. Nonlinear scale space with spatially varying stopping time. *IEEE Trans. Pattern Anal. Machine Intell.* 30 (12), 2175–2187.
- Gilboa, G., Sochen, N., Zeevi, Y., 2004. Image enhancement and denoising by complex diffusion process. *IEEE Trans. Pattern Anal. Machine Intell.* 25, 1020–1036.
- Jobson, D., Rahman, Z., Woodell, G., 1997. A multiscale retinex for bridging the gap between color images and the human observation of scenes. *IEEE Trans. Image Process.* 6 (7), 965–976.
- Koenderink, J., Van Doorn, A., 1984. The structure of images. *Biological Cybernet.* 363–370.
- Lee, J., 1986. Speckle suppression and analysis for synthetic aperture radar. *Opt. Eng.* 25 (5), 636–643.
- Lindberg, T., 1996. Edge detection and ridge detection with automatic scale selection. In: *Proc. IEEE Comput. Society Conf. on Computer Vision and Pattern Recognition*, pp. 465–470.
- Ling, J., Bovik, A., 2002. Smoothing low-SNR molecular images via anisotropic median diffusion. *IEEE Trans. Med. Imaging* 21, 377–384.
- Lopes, A., Nezry, E., Touzi, R., Laur, H., 1993. Structure detection and adaptive speckle filtering in SAR Images. *Internat. J. Remote Sens.* 14 (9), 1735–1758.
- Maeda, J., Iizawa, T., Ishizaka, T., Ishikawa, C., Suzuki, Y., 1998. Segmentation of natural images using anisotropic diffusion and linking of boundary edges. *Pattern Recognition* 31, 1993–1996.
- Manmatha, R., Rothfeder, J., 2005. A scale space approach for automatically segmenting words from historical handwritten documents. *IEEE Trans. Pattern Anal. Machine Intell.* 27 (8), 1212–1225.
- Pathak, S., Chalana, V., Haynor, D., Kim, Y., 2000. Edge-guided boundary delineation in prostate ultrasound images. *IEEE Trans. Med. Imaging* 19, 1211–1219.
- Perona, P., Malik, J., 1990. Scale-space and edge detection using anisotropic diffusion. *IEEE Trans. Pattern Anal. Machine Intell.* 12 (7), 629–639.
- Petrovic, A., Divorra, O., Vanderghynst, P., 2004. Multiresolution segmentation of natural images: From linear to nonlinear scale-space representations. *IEEE Trans. Image Process.* 13 (8), 1104–1114.
- Sobol, I., 1997. Uniformly distributed sequences with an additional uniform property. *USSR Comput. Math. Math. Phys.* 16, 236–242.
- von Neumann, J., 1951. Various techniques used in connection with random digits. *National Bureau of Standards. Appl. Math. Series* 12, 36–38.
- Witkin, A., 1983. Scale–scale filtering. In: *Proc. 7th Internat. Joint Conf. on Artificial Intelligence*, pp. 1019–1022.
- Wong, A., Mishra, A., Yates, J., Clausi, D.A., Fieguth, P., Callaghan, J., 2009. Intervertebral disc segmentation and volumetric reconstruction from peripheral quantitative computed tomography imaging. *IEEE Trans. Biomed. Eng.* 56 (11), 2748–2751.
- Yu, J., Wang, Y., Shen, Y., 2008. Noise reduction and edge detection via kernel anisotropic diffusion. *Pattern Recognition Lett.* 29, 1496–1503.